

1 **Thermal characteristics of permafrost in the steep alpine rock**
2 **walls of the Aiguille du Midi (Mont Blanc Massif, 3842 m a.s.l)**

3

4 **F. Magnin¹, P. Deline¹, L. Ravanel¹, J. Noetzli², P. Pogliotti³**

5 [1]{EDYTEM Lab, Université de Savoie, CNRS, Le Bourget-du-Lac, France}

6 [2]{Glaciology and Geomorphodynamics Group, Department of Geography, University of
7 Zurich, Zurich, Switzerland}

8 [3]{ARPA Valle d'Aosta, Saint-Christophe, Italy}

9

10 Correspondence to:

11 F. Magnin (florence.magnin@univ-savoie.fr)

12 P. Deline (philip.deline@univ-savoie.fr)

13 L. Ravanel (ludovic.ravanel@univ-savoie.fr)

14 J. Noetzli (jeannette.noetzli@geo.uzh.ch)

15 P. Pogliotti (paolo.pogliotti@gmail.com)

16 **Abstract**

17 Permafrost and related thermo-hydro-mechanical processes are thought to influence high
18 alpine rock wall stability, but a lack of field measurements means that the characteristics and
19 processes of rock wall permafrost are poorly understood. To help remedy this situation, in
20 2005 work began to install a monitoring system at the Aiguille du Midi (3842 m a.s.l). This
21 paper presents temperature records from nine surface sensors (eight years of records) and
22 three 10-m-deep boreholes (four years of records), installed at locations with different surface
23 and bedrock characteristics. In line with previous studies, our temperature data analyses
24 showed that: micro-meteorology controls the surface temperature, active layer thicknesses are
25 directly related to aspect and ranged from <2 m to nearly 6 m, and that thin accumulations of
26 snow and open fractures are cooling factors. Thermal profiles empirically demonstrated the
27 coexistence within a single rock peak of warm and cold permafrost (about -1.5°C to -4.5°C at
28 10-m-depth) and the resulting lateral heat fluxes. Our results also extended current knowledge
29 of the effect of snow, in that we found similar thermo-insulation effects as reported for gentle
30 mountain areas. Thick snow warms shaded areas, and may reduce active layer refreezing in
31 winter and delay its thawing in summer. However, thick snow thermo-insulation has little
32 effect compared to the high albedo of snow which leads to cooler conditions at the rock
33 surface in areas exposed to the sun. A consistent inflection in the thermal profiles reflected the
34 cooling effect of an open fracture in the bedrock, which appeared to act as a thermal cutoff in
35 the sub-surface thermal regime. Our field data are the first to be obtained from an Alpine
36 permafrost site where borehole temperatures are below -4°C , and represent a first step
37 towards the development of strategies to investigate poorly known aspects in steep bedrock
38 permafrost such as the effects of snow cover and fractures.

39

40 **1 Introduction**

41 The last few decades have seen an increase in rockfall activity from steep, high-altitude rock
42 walls in the Mont Blanc Massif (Western European Alps) (Ravanel and Deline, 2010; Deline
43 et al., 2012). Several studies of recent rock avalanches and rockfalls in mid-latitude alpine
44 ranges have ascribed such increases to climate-related permafrost degradation (Deline, 2001;
45 Gruber et al., 2004a; Huggel et al., 2005; Fischer et al., 2006; Huggel et al., 2008; Allen et al.,
46 2009; Ravanel et al., 2010, 2012; Deline et al., 2011). Rockfall magnitude and frequency are
47 thought to be linked to the timing and depth of permafrost degradation, which can range from

48 a seasonal deepening of the active layer to long-term, deep-seated warming in response to a
49 climate signal (Gruber and Haeberli, 2007). Local warming of cold permafrost may be
50 induced by advection and the related erosion of cleft ice (Hasler et al., 2011b), which can lead
51 to unexpected bedrock failures. As Krautblatter et al. (2011) noted, before being able to
52 predict permafrost-related hazards, it is necessary to develop a better understanding of the
53 thermo-hydro-mechanical processes involved, which means collecting rock temperature
54 measurements and developing modeling strategies.

55 Measurement strategies and numerical experiments have been used to investigate the thermal
56 conditions and characteristics of near-vertical and virtually snow-free alpine rock walls that
57 are directly coupled with the atmosphere (Gruber et al., 2003; 2004b, Noetzli et al., 2007).
58 These studies have shown the domination of topographical controls on steep bedrock
59 permafrost distribution, with a typical surface temperature difference of 7-8°C between south
60 and north-facing slopes, the possible coexistence of warm and cold permafrost in a single rock
61 mass, and lateral heat fluxes within the rock mass inducing near-vertical isotherms. Hasler et
62 al. (2011a) suggested that, both thin accumulations of snow on micro-reliefs and cleft
63 ventilation may cause deviations of 1°C (shady faces) to 3°C (sunny faces) compared with the
64 smooth, snow-free rock wall model test cases. The thermal influence of snow on steep rock
65 faces has been addressed *via* numerical experiments (Pogliotti, 2011), which have shown that
66 the effect of snow is highly variable and depends on topography, and the depth and timing of
67 the accumulation. However, few empirical data are available to evaluate numerical
68 experiments. Recent advances in the study of steep alpine rock walls have helped to build
69 bridges between what is known about the general characteristics of permafrost and processes
70 related to the microtopography and internal structure of rock masses, which may be
71 significant in their short-term evolution and in permafrost distribution. However, a much
72 larger corpus of field observations and monitoring data for a variety of bedrock conditions is
73 needed to develop, calibrate, and evaluate reliable models.

74 As part of our research into geomorphic activity in the Mont Blanc Massif, in 2005 we started
75 a long-term permafrost-monitoring program at the Aiguille du Midi (AdM), currently the
76 highest instrumented bedrock permafrost site in the European Alps (3842 m a.s.l). This
77 monitoring program was designed to characterize and determine the thermal state of the
78 permafrost and active layer, and to collect temperature data under variable snow-cover and
79 structural conditions that could be used to calibrate and validate high-resolution numerical
80 experiments on permafrost thermal processes.

81 In this paper we describe the monitoring program at the AdM, and present temperature data
82 from nine surface mini-loggers and three 10-meter-deep boreholes. Due to the morphology of
83 the AdM, the monitoring network is concentrated in a very small area; however the data
84 obtained allowed us to address the following questions:

85 - How much of the surface temperature variability over this small area is due to topography
86 and snow cover?

87 - How much of the variability in the active layer is due to the topography of the steep rock
88 walls?

89 - What are the thermal effects of snow and fractures on sub-surface temperatures at the AdM?

90 We used eight years of surface records and four years of borehole to analyze seasonal and
91 annual variations in temperature patterns, in the active layer, and in the permafrost thermal
92 regime. We discuss our results in the light of previous research and provide new empirical
93 evidence for the effects of snow and fractures on permafrost in steep rock walls.

94

95 **2 Study site**

96 The AdM lies on the NW side of the Mont Blanc Massif (Fig. 1). Its summit (45.88° N,
97 6.89°E) consists of three granite peaks (Piton Nord, Piton Central, and Piton Sud) and
98 culminates at 3842 m a.s.l. The steep and partly glaciated north and west-facing slopes of the
99 AdM tower more than 1000 m above the Glacier des Pèlerins and Glacier des Bossons, while
100 its south-facing slope rises just 250 m above the Glacier du Géant (i.e., the accumulation zone
101 of the Mer de Glace). This part of the Mont Blanc Massif is formed by an inclusion-rich,
102 porphyritic granite and is bounded by a wide shear zone. A main, N 40°E fault network
103 intersected by a secondary network determines the distribution of the main granite spurs and
104 gullies (Leloup et al., 2005). The highest parts of the peak tend to be steep, contain few large
105 fractures, and, in places, are characterized by vertical foliation bands and small fissures. The
106 lower parts are less steep and more fractured. In the present paper we use the abbreviation
107 AdM to refer only to the upper section of the Piton Central, between 3740 and 3842 m a.s.l.
108 where most of the instruments are installed. A tourist cable car runs from Chamonix to the
109 Piton Nord. Galleries and an elevator allow visitors to gain the viewing platform on top of the
110 Piton Central, from where there is a 360° panorama of the Mont Blanc Massif.

111 We chose the AdM as a monitoring site for the following scientific and logistical reasons: (i)
112 permafrost is extremely likely due to the AdM's high altitude and the presence of cold-based
113 hanging glaciers on its north-facing slope; (ii) the morphology of the peak offers a range of
114 aspects, slope angles, and fracture densities that are representative of many other rock walls in
115 the massif; (iii) the easy access by cable-car from Chamonix and the availability of services
116 (e.g., electricity) at the summit station. Monitoring equipment was installed as part of the
117 *PERMAdataROC* (2006–2008) and *PermaNET* (2008–2011) projects, funded by the
118 European Union and run jointly by EDYTEM Lab (France), ARPA VdA (Italy), and the
119 Universities of Zurich (Switzerland), Bonn, and Munich (Germany). As such, it complements
120 other rock wall observation sites, for example, those within the Swiss Permafrost Monitoring
121 Network (PERMOS).

122 Data from the monitoring equipment on the AdM was completed by data from ARPA VdA's
123 weather stations, which measured air temperature and relative humidity, incoming and
124 outgoing shortwave and longwave solar radiation, wind speed, and wind direction on the
125 south and north-facing slopes between 2006 and 2010. Electrical Resistivity Tomography
126 (ERT) and Induced Polarization (IP) have been measured since 2008 in conjunction with the
127 Universities of Bonn and Munich. High-resolution (cm-scale) triangulated irregular networks
128 (TIN) of rock walls and galleries of the AdM were obtained from terrestrial laser scanning. In
129 July 2012, six crack-meters equipped with wireless sensors were installed in major fractures
130 in the Piton Central and Piton Nord in order to complement existing studies of cleft dilatations
131 and shearing movements in rock wall permafrost, to check the stability of the AdM and to test
132 an early warning system. Finally, two GPR surveys were performed along vertical transects in
133 2013 and 2014. Not all of these data were used in the present study but they will contribute to
134 future research.

135

136 **3 Data collection methods**

137 **3.1 Rock temperature monitoring**

138 The present study was based on rock surface temperatures taken at the top of the AdM
139 (between 3815 and 3825 m a.s.l.; Fig. 2) since 2005 by a network of mini-loggers
140 (GeoPrecision PT1000 sensors, accuracy $\pm 0.1^\circ\text{C}$) installed by the University of Zurich and
141 ARPA VdA. Two loggers were installed in snow free locations on each face of the AdM
142 (Table 1). The south-facing slope has an additional logger (S3) installed just above a small

143 ledge on which snow accumulates in winter, covering the logger. The loggers record the
144 temperature every hour at depths of 0.03, 0.30, and 0.55 m, in line with the method described
145 by Gruber et al. (2003).

146 In September 2009, three boreholes were drilled in the lower section of the Piton Central, at
147 between 3738 and 3753 m a.s.l.

148 In order to minimize possible thermal disturbances caused by air ventilation in the galleries
149 and heating from staff rooms, the boreholes were drilled several tens of meters below the
150 galleries running through the AdM. The criteria used to decide the exact location of each
151 borehole were the aspect, fracturing, roughness, and angle of the rock wall (Fig. 2). Each
152 borehole was drilled perpendicular to the rock surface and to a depth of 11 meters. Borehole
153 depths were constrained by the drilling equipment and the funding available. The boreholes
154 on the northeast (BH_E) and south-facing (BH_S) slopes were drilled in fractured rock walls
155 that slope at 65° and 55°, respectively. Even on rock walls at these angles, snow can
156 accumulate on the micro-reliefs in the face. The borehole on the northwest-facing slope
157 (BH_N) was drilled in a vertical, unfractured wall. The only place that snow can accumulate
158 on this wall is on small ledges such as the one above which BH_N was drilled.

159 The boreholes were drilled between September 14th and September 27th, 2009 by a team of
160 five people (two mountain guides, plus three members of the EDYTEM Lab) who had to
161 contend with very variable weather and challenging logistics. For each borehole it was
162 necessary to: (i) install a safety line for the workers, (ii) set up a rope system to carry the
163 equipment from the galleries to the drill site, (iii) install a work platform for the three drillers,
164 (iv) anchor a base on which to fix a rack way, (v) drill the hole using a 380-V Weka
165 Diamond-Core DK 22 electric drill, (vi) insert into the hole a polyethylene PE100 tube (outer
166 diameter: 40 mm; inner diameter: 29 mm) sealed at its bottom, and (vii) remove the work
167 platform. In addition to the difficult environment and harsh weather, the drilling work was
168 complicated by the heterogeneity and hardness of the granite, which took a heavy toll on the
169 equipment (11 diamond heads worn out or broken, a dozen steel tubes damaged, and a motor
170 broken). At first we tried to drill 46-mm-diameter boreholes but we had to increase the
171 diameter to 66 mm so we could use a more robust pipe string. Cooling required 1 to 3 m³ of
172 water per day, which was carried up from Chamonix in 1-m³-tanks via the cable car. Space
173 between the drill hole and the casing was not filled.

174 The three boreholes were fitted with 10-m-long Stump thermistor chains, each with 15-nodes
175 (YSI 44031 sensors, accuracy $\pm 0.1^\circ\text{C}$) arranged along a 6-mm fiberglass rod. Following

176 calibration at 0°C in an ice-water basin, the sensors were inserted in BH_S and BH_N in
177 December 2009 and in BH_E in April 2010 (Fig. 3). In order to prevent heat convection, each
178 sensor was separated from the others on the chain by insulating foam. The boreholes were
179 closed at the top, but the chains can be removed to check for thermistor drift. Rock
180 temperatures at depths between 0.3 and 10 m are recorded every three hours (Table 1).
181 Because BH_S is shallower than 10 m, the thermistor chain protrudes from the rock surface
182 by 36 cm. Temperature comparisons between BH_S and BH_N/BH_E were carried out at the
183 closest equivalent depths (*e.g.*, temperatures at a depth of 2.64 m in BH_S were compared
184 with temperatures at a depth of 2.5 m in BH_E and BH_N).

185

186 **3.2 Air temperature and snow cover measurements**

187 In order to aid interpretation of the rock temperature data, we collated air temperature data
188 (AT, Table 1) collected by Météo France at a station 3 m above the top of the Piton Central
189 (3845 m a.s.l.) since 2007. Data prior to 2007 (1989–2006) are very fragmented due to
190 insufficient equipment maintenance and are not used in this study.

191 Two automatic cameras have taken six pictures per day of the south and northeast borehole
192 sites since January 2012. In addition, five graduated stakes were placed around each borehole
193 in order to evaluate the spatial variability of snow accumulation from the photographs. Visual
194 analysis of the photos taken during the winters of 2012 and 2013 showed a thick spatially
195 homogeneous snow cover (>1m), which lasted until late spring at BH_S, and a thin (<0.5 m)
196 spatially variable snow cover at the BH_E, where the rock face is much steeper and more
197 complex (Table 1). Snow accumulations at BH_N and S3 were estimated from field
198 observations. Accumulations of snow at BH_N were restricted to the relatively large ledge
199 above which the borehole is drilled. This snow patch was over 1-m-thick for most of the year.
200 S3 is also frequently covered by >0.5 m of snow, which accumulates during winter and spring
201 on the small ledge above the sensor. Snow depth is more variable at S3 than at BH_N because
202 the intense solar radiation at S3 leads to more frequent melting.

203

204 **4 Dataset preparation**

205 The borehole time series were all continuous except for short periods for BH_S, as this logger
206 was removed from September 2012 to January 2013 and from October 2013 to January 2014

207 to prevent it being damaged by engineering work close to the borehole. Gaps in the 0.3-m
208 temperature and AT time series were filled in so we could calculate seasonal and annual
209 means (cf. Table 2). First, we calculated daily means from rock temperature time series for
210 days with complete records. Then, we filled short gaps (<5 days) by linear interpolation
211 between the nearest available data points for the same depth. Longer gaps (up to 1.5 month)
212 were filled by replacing missing data with the average value for the 30 days before and 30
213 days after the gap (cf. Hasler et al., 2011a). To fill the longest gaps for E1, N1, S1, and W1
214 (from December 4th, 2007 to February 7th, 2008) we used a third approach that involved
215 applying a linear regression equation, fitted using data from each pair of loggers (e.g., E2 and
216 E1) and records for the missing periods (*i.e.*, December-February) from groups of years with
217 complete records (2006–2007 and 2008–2009). Correlation coefficients for the equations
218 ranged from 0.89 (S1 and S2) to 0.94 (E1 and E2). We tested this approach by simulating
219 corresponding gap periods in the years with complete data and then filling these gaps using
220 the regression equations. Differences between the annual means obtained using this method
221 and the annual means calculated from the complete data set were in the range 0.01–0.15°C
222 and can be considered negligible. Our calculations of seasonal means did not include data
223 obtained using the 30-day average or linear regression methods. The longest gap we filled in
224 any one year was <1.5 months, in line with standard practice for the PERMOS network
225 (personal communication).

226

227 **5 Rock surface temperature**

228 Smith and Riseborough (2002) defined Surface Offset (SO) as the difference between local air
229 temperature and ground surface temperature. SO is a parameter in the TTOP model
230 (Temperature at the Top of Permafrost, Smith and Riseborough, 1996), originally developed
231 to define the functional relation between air and ground temperatures in polar lowlands and
232 later applied to high-latitude mountainous terrain (Juliussen and Humlum, 2007). SO can be
233 used to quantify the overall effect of ground cover and ground surface parameters on the
234 surface energy balance.

235 We calculated annual SOs (ASO), using Mean Annual Air Temperature (MAAT) and Mean
236 Annual Ground Surface Temperature (MAGST), and seasonal SOs (SSO) from seasonal
237 means for winter (December to February), spring (from March to May), summer (from June
238 to August), and fall (from September to November), using time series measured at depths of
239 0.3-m (boreholes and E2, S2, W2, N2) and 0.1-m (E1, S1, W1, N1) - points we considered

240 representative of surface conditions. We applied a standard lapse rate of $0.006^{\circ}\text{C}\cdot\text{m}^{-1}$ to air
241 temperatures in order to balance the elevation difference between the Météo France station
242 and the sensors. Figure 4 shows ASOs for all the complete years (Fig. 4A), SSOs for snow-
243 free sensors for the available seasons (Fig. 4B), and SSOs for snow-covered sensors for the
244 available seasons (Fig. 4C). We also analyzed daily temperature records for the snow covered
245 sensors and air temperature trends as part of our investigation of the effect of snow cover on
246 snow temperatures (Fig. 5).

247

248 **5.1 Surface Offset patterns**

249 Maximum and minimum ASOs were 9.3°C at S1 in 2011, and 1.3°C at N1 in 2009 (Fig. 4A).
250 These are typical values for the Alps (PERMOS, 2013). On the south-facing slope, the snow-
251 covered sensors gave lower values than the snow-free sensors. For example, the ASOs for S3
252 were between 0.1°C (2010) and 1.4°C (2011) lower than the ASOs for S1. Conversely, on the
253 north side, the snow-covered sensor gave higher ASOs than the snow-free sensors. On a
254 seasonal timescale, the maximum SSOs occurred in summer for the snow-free sensors (Fig.
255 4B), except for the sensors on the south-facing slope (S1 and S2), where the maximum SSOs
256 occurred in spring, with values $>10^{\circ}\text{C}$. The lowest SSOs were recorded in winter, and ranged
257 from approximately 8°C on the south-facing slope to $<1^{\circ}\text{C}$ on the north-facing slope (N1 and
258 N2). SSO patterns for the snow-covered sensors (Fig. 4C) were opposite to those for the
259 snow-free sensors, except for BH_E. At BH_N and BH_S, SSOs were largest in winter (4.1°C
260 and 9.5°C , respectively) and lowest in summer. At S3, the largest SSO was in the fall. Fall
261 SSOs were also relatively high at BH_N and BH_S. In contrast to SSOs at other snow-
262 covered sensors, SSOs at BH_E followed a similar pattern to that recorded at the snow-free
263 sensors, in that SSO values were directly related to insolation duration.

264 From 2011 to 2012, the changes in ASO at snow-covered and shady sensors such as BH_E
265 and BH_N were greater ($+1.1^{\circ}\text{C}$) than they were at the snow-covered and south-facing
266 sensors (only $+0.3^{\circ}\text{C}$ at S3). Conversely to the snow-covered sensors, the ASO decreased at
267 the snow-free sensors from 2011 to 2012, with, for example, values of -1°C at S2 and -0.3°C
268 at E1. The maximum and minimum ASOs for the different snow-free sensors varied with
269 aspect, with, for example, maximum ASOs in 2008 at W1 and W2, but in 2011 at S1 and S2.

270

271 **5.2 Daily temperatures at snow-covered sensors**

272 Daily temperature curves for the snow-covered sensors are smoothed compared to air
273 temperature oscillation during cold periods (Fig. 5). The S3 and BH_S temperature curves
274 were strongly smoothed from mid-November 2010 to January (BH_S) or April 2011 (gap for
275 S3), and from early December 2011 to mid-May 2012. Both sensors recorded a period of
276 almost constant 0°C conditions from April to mid-May 2012. The temperature curve for
277 BH_N was strongly smoothed until the summer, with a similar constant 0°C period for three
278 weeks in July 2011. Although the BH_E temperature curve from late September to February-
279 March was mostly smoother than daily air temperature curve, the two curves were more
280 closely coupled than they were at the other sensors, as the oscillations in temperatures at
281 BH_E were in-synch with major changes in AT, such as the large drop in temperature in
282 December 2012. From September 2010 to March 2011 and from November 2011 to February
283 2012, the temperatures recorded at BH_E were lower than those recorded at BH_N.

284

285 **5.3 Snow cover and micro-meteorological influences**

286 Normally on steep, snow-free bedrock in the high mountains, the MAGST is higher than
287 MAAT, mainly because of direct solar radiation (Gruber et al. 2004b) but also due to a
288 contribution from reflected solar radiation from large, bright glacier surfaces below
289 measurement points (PERMOS, 2013). In the European Alps, the ASO can be up to 10°C on
290 south-facing rock walls, whereas the maximum ASO values recorded on steep rock walls in
291 Norway are only 3°C, as there is less direct solar radiation at higher latitudes (Hipp et al.,
292 2014). In New Zealand, at similar latitude to the Alps, Allen et al. (2009) reported a
293 maximum ASO value of 6.7°C. This lower value is probably the result of reduced direct solar
294 radiation due to the influence of the oceanic climate and related frequent cloud cover. Most of
295 the surface sensors used in the above studies were installed in snow-free conditions in order to
296 test energy balance models (Gruber et al., 2004b) or for statistical fitting (Allen et al., 2009,
297 Boeckli et al., 2012). At the AdM, the ASO patterns of snow-covered sensors at snow-
298 covered sensors differed from those at snow-free sensors, mainly due to decoupling from
299 atmospheric conditions during the winter season and the lower surface albedo of the snow-
300 free sensors.

301 The differences in ASOs between snow-covered and snow-free sensors on similar aspects
302 show that snow has a substantial effect on the annual energy balance. According to empirical

303 and numerical studies (Hanson and Hoelzle, 2004; Luetschg et al., 2008), snow cover must be
304 at least 0.6-0.8-m-thick to insulate the rock surface from the air temperature, but snow cover
305 on steep rock walls is usually thinner than this insulating threshold (Gruber and Haeberli,
306 2009). The differences between BH_N and BH_E in terms of ASOs and SSOs can probably
307 be ascribed to variations in mean snow cover thickness (Table 1), and demonstrate that the
308 insulating effect of snow can occur locally also in steep rock walls. On the north-facing slope,
309 ASOs were higher at snow-covered sensors (BH_N) than at snow-free sensors (N1 and N2),
310 showing that thermo-insulation by snow significantly increases the MAGST. On the south-
311 facing slope, ASOs were lower at the snow-covered sensors (BH_S and S3) than at the snow-
312 free sensors (S1 and S2), indicating that snow lowers the MAGST. This reduced warming
313 effect could result from the combination of (i) thin snow cover with negligible thermo-
314 insulation, (ii) a higher surface albedo, (iii) and melt energy consumption (Harris and Corte,
315 1992; Pogliotti, 2011). The latter two factors seem to be prevalent at the AdM because snow
316 cover on the south-facing slope is often greater than 1-m-thick during winter (sect 3.2) leading
317 to a marked smoothing of daily temperature oscillations (Fig. 5). These results extend
318 previous studies on thin snow accumulations (Hasler et al. 2011a). The importance of this
319 reduced warming effect on sunny faces is probably reinforced by the fact that snow is present
320 for much of the year at such altitudes, as suggested by (i) the high fall SSOs (early snow
321 accumulation) for snow-covered sensors, (ii) their low summer SSOs, and (iii) by the nearly-
322 constant temperature close to 0°C in late summer (Fig. 5). This constant 0°C temperature may
323 reflect the zero-curtain effect, which results in the snow melting and retards the thawing of the
324 active layer, as has been described for snow-covered gentle mountain slopes (e.g. Hanson and
325 Hoelzle, 2004; Gubler et al., 2011).

326 Various interannual differences were recorded at snow-covered and snow-free sensors. The
327 PERMOS study (2013) has reported analogous variability in interannual differences between
328 rock walls and gentle snow-covered terrain. Interannual differences at the snow-free sensors
329 were mainly related to differences in insolation due to cloud cover. It may be that variability
330 in interannual differences from one aspect to another are also due to variations in cloud
331 formation from year-to-year. Energy balance models have shown that convective cloud
332 formation can cause differences in the spatial distribution of MAGST over a single rock peak
333 (Noetzli et al., 2007). On shady faces, the effect of solar radiation control is greatly reduced
334 and snow cover may be the most important factor affecting interannual differences.
335 Consequently, the temperature at a snow-covered sensor can increase from one year to the

336 next if snow insulation from the atmospheric temperature increases, while the temperature at a
337 snow-free sensor may drop due to reduced insolation. In the case of sun-exposed and snow-
338 covered sensors, such as S3, the balance between warming and cooling effects leads to
339 smaller interannual ASO differences than at sensors in shadier locations, where temperature
340 are mostly controlled by the warming effect of snow insulation. Thus, the influence of snow
341 cover on the surface temperature of high-altitude rock walls is a due to a combination of
342 topography, snow depth, and micro-meteorology.

343

344 **6 Borehole records**

345 Four years of data from the three boreholes allowed us to describe daily temperature patterns
346 (Fig. 6), mean annual Temperature-Depth ($T(z)$) profiles, and annual temperature envelopes
347 (*i.e.*, the maximum and minimum daily temperatures at each depth in 2011; Fig. 7). We
348 focused on the active layer and the permafrost thermal regime, paying special attention to
349 thermal effects related to snow cover and bedrock structure. We discuss their possible
350 influence on the active layer and bedrock thermal regime.

351

352 **6.1 Active layer**

353 Active Layer Thickness (ALT) varied with aspect, with means of ca. 3 m at BH_E, 5.5 m at
354 BH_S, and 2.2 m at BH_N (Fig. 6). Interannual variability during the monitoring period was
355 ca. 0.7 m for each borehole (Table 3). Maximum ALTs occurred in 2012 at BH_N (2.5 m
356 deep) and in 2013 at BH_E (3.4 m deep). At BH_S, data are missing for 2012 and 2013, but
357 2010 and 2011 data show a maximum ALT in 2011 of 5.9 m. The length of the thawing
358 period, marked by continuous positive temperatures at the uppermost thermistor, also varied
359 according to aspect. It was longest at BH_S, starting in June (April in 2011), but with isolated
360 thawing days already in March (*e.g.*, in 2012). In general, the surface at BH_S refroze in
361 October, but total refreezing of the active layer did not occur until December in 2010 and
362 2011. The 2011–2012 freezing period was particularly mild and short (3–4 months) at BH_S.
363 This pattern was not as marked at BH_E, which even recorded its lowest surface temperature
364 in 2011–2012. BH_N had the longest freezing periods because temperatures in the rock sub-
365 surface remained positive only from June to October. In 2011, thawing did not start until
366 August. BH_E had the most balanced thawing and freezing periods (ca. 6 months each).

367 The timing of maximum ALT depended on aspect and year (Table 3). In 2010 and 2011,
368 maximum ALT occurred earliest at BH_E, even though the active layer was thicker at BH_E
369 than at BH_N. In 2012 and 2013, BH_N was the first site to reach maximum ALT. In 2010,
370 maximum ALT at BH_S occurred very late, three months after BH_E. Although the BH_S
371 active layer had mostly thawed by mid-July, thawing continued steadily until the end of
372 October. Maximum ALT always occurred later at BH_S than at the other boreholes, but the
373 lowering of the 0°C isotherm was more linear.

374

375 **6.2 Thermal regime**

376 Annual Temperature-Depth T(z) profiles (Fig. 7A) revealed different thermal regimes. The
377 AdM's Piton Central has both warm (ca. -1.5°C at BH_S) and cold (ca. -4.5°C at BH_N)
378 permafrost (Table 3). Interannual changes were not similar in every borehole. In BH_N and
379 BH_E, the changes over 2010-2013 generally followed the changes in MAAT all along the
380 T(z) profiles. For example, the T(z) profiles show considerable warming from 2010 to 2011 in
381 response to the 2.3°C rise in MAAT (Table 3). The BH_N T(z) profile in 2011 was
382 significantly warmer than in other years for depths up to 2.5 m; however it was colder than
383 2012 for depths greater than 3 m and colder than 2013 for depths greater than 7 m. In BH_S,
384 the mean annual T(z) profile for 2011 showed remarkably high temperature near the surface
385 with positive temperatures up to a depth of 1 m. Temperatures were higher than in 2010 for
386 the shallowest 6 m of the profile but slightly lower than in 2010 below this depth.

387 The zero annual amplitude depth is >10 m for every borehole (Fig. 7B), which is consistent
388 with other bedrock sites in the European Alps (PERMOS, 2007). In 2011, the largest
389 amplitudes in daily temperature (peak to peak) at the surface (>20°C) and at 10 m depth
390 (1.6°C) were at BH_E, and the smallest surface (15.5°C) and 10-m (1.0°C) amplitudes were
391 at BH_N and BH_S, respectively. In line with the surface pattern, the minimum T(z) profile
392 from the surface to 1.4-m depth was warmer at BH_N than at the sunnier BH_E (Fig. 7B).

393 The minimum and mean annual T(z) profiles for BH_N contain two distinct sections
394 separated by an inflection at ca. 2.5 m deep (Fig. 7A). This coincides with an 8–10 cm-wide
395 cleft encountered at this depth during the drilling operation. The temperature gradient is
396 negative (-0.39°C m⁻¹) from the surface to the cleft, and then positive from the cleft to 10-m-
397 deep (from 0.16°C m⁻¹ to nearly isothermal). The mean annual profiles for BH_E are almost
398 linear and have a temperature gradient of ca. -0.02°C m⁻¹. In the case of BH_S, the upper

399 parts of the annual T(z) profiles for 2010 and 2011 differ greatly, with an almost linear
400 temperature gradient of $-0.07^{\circ}\text{C m}^{-1}$ in 2010, and a much steeper overall temperature gradient
401 of $-2.26^{\circ}\text{C m}^{-1}$ in 2011.

402

403 **6.3 Snow cover and bedrock discontinuity controls**

404 The coexistence of warm and cold permafrost, and the opposite temperature gradients at
405 BH_S and BH_N, probably due to lateral heat fluxes, are in accordance with the results of
406 numerical simulations (Noetzli et al. 2007).

407 In terms of the permafrost thermal regime, the values recorded at BH_N were below -4°C ,
408 which is a value typical for high latitude monitoring sites, such as those in Svalbard (Noetzli
409 et al., 2014a), and the warmest boreholes of the continuous permafrost zone in Alaska
410 (Romanovsky et al., 2014).

411 The spatial and temporal variability of ALT is consistent with values reported for Swiss
412 boreholes in bedrock (PERMOS, 2013). For example, the thickness and timing of the ALT in
413 BH_E are similar to those recorded at the Matterhorn-Hörnligrat site (3295 m a.s.l, vertical
414 borehole on a crest), with values ranging from 2.89 to 3.66 m between 2008 and 2010, and
415 with maximum ALT occurring between early September and early October. Early studies
416 considered that in bedrock slopes, changes in ALT are strongly controlled by summer air
417 temperature, as indicated by the ALT at Schilthorn (2909 m a.s.l) which was twice as thick as
418 usual (from 4-5 m to > 8 m) during the hot summer of 2003, while there was no unusual
419 increase in the ALT under the debris-covered slopes, such as Les Gentianes moraine and the
420 Arolla scree slopes, located in the same area and at similar altitude (PERMOS, 2013).

421 The different patterns of ALT variability at the three AdM boreholes (Table 3) suggest that
422 the air temperature is not the only controlling factor. The relatively mild and short 2011–2012
423 freezing period at BH_S may have been due to snow insulation, as suggested by the
424 subsequent period of constant temperature from the surface to a depth of 3 m (Fig. 6). This
425 isothermal period coincided with the zero-curtain effect observed at the surface temperature
426 from April to mid-May 2012 (see sections 5.2 and 5.3, Fig. 5). As reported by Hoelzle et al.,
427 (1999), thick, long lasting snow cover reduces both freezing of the active layer by insulating it
428 from low temperatures and thawing of the active layer by late snow melting. Such an effect on
429 the active layer freeze-thaw cycles has been reported by studies in gentle mountain terrains,
430 but has not been observed in steep bedrock permafrost (Gruber et al. 2004a). A comparison of

431 temperature variations at BH_E and BH_N clearly shows the effect of snow insulation (Fig.
432 5). Most notably, winter surface temperatures are always warmer and smoother at BH_N than
433 at BH_E (Fig. 5) and at depth (Fig. 7B). Snow appears to have a warming effect at depths of
434 up to 1.4 m. In terms of ALT, the different trends between BH_E and BH_N during the period
435 2011-2013 (Table 3) may be due to the effect of long-lasting snow cover at BH_N modifying
436 its response to the climate signal. Conversely, the reduced ALT at BH_E in 2011, in contrast
437 with BH_S and BH_N, may be the result of variations in the effect of summer snow fall on
438 these different faces. Unfortunately, the cameras and snow stakes that would have allowed us
439 to check this hypothesis were not installed in 2012 (sect. 3.2). Further studies are needed to
440 verify this hypothesis.

441 According to a modelling study, the interannual variability of ALT is greater on sun-exposed
442 faces, as they respond as much to change in air temperature as to changes in solar radiation
443 (Gruber et al. 2004a). However, our data did not conform to this prediction, as the change in
444 ALT at BH_S was similar to the ALTs at the shadier BH_E and BH_N. Furthermore, BH_S
445 experienced the smallest interannual changes at 10-m-depth, and the shape of its T(z) profiles
446 between 2010 and 2011 did not follow the trend of the MAAT signal at depths between 6 and
447 10 m. This may be due to the consumption of latent heat. In fact, previous studies have
448 attributed the delaying and dampening effect of latent heat consumption to the thermal
449 response of bedrock permafrost (Kukkonen et Safanda, 2001; Wegmann et al. 1998, Noetzli
450 et al. 2007). Field observations during drilling revealed the presence of wet-detritic materials
451 in the fractures in BH_S, suggesting that latent heat may be consumed by phase changes
452 between interstitial water and ice during phase-change. Evidence for latent heat consumption
453 at BH_S is supported by the temperatures in the borehole, which are around the values
454 required for phase-change processes. Snow accumulation and melting on the south-facing
455 slope are an obvious source of water to supply bedrock discontinuities.

456 Interannual changes at BH_E and BH_N followed variations in MAAT all along their profiles
457 (except for BH_N in 2011) suggesting that latent heat consumption did not occur (Fig. 7A).
458 From 2010 to 2011 the BH_N T(z) profile warmed significantly above the cold inflection.
459 This followed MAAT (Table 3), but the colder conditions below the inflection were not in
460 accordance with the climate signal. Hence, the fracture seems to act as a thermal cutoff
461 between the surface layer and the deep bedrock. The sharp inflection in the profiles at the
462 fracture depth, which is especially prominent in the mean and minimum annual T(z) profiles,
463 indicates that the fracture locally cools the rock. Mean annual temperature is even lower at

464 depth of 2.5 m than it is at the surface, which, as explained above, is probably insulated by the
465 snow cover. Seasonal temperature profiles for BH_N (Fig. 8) show a relatively large
466 difference between the temperature gradient above and below the fracture depth during winter
467 (Dec. to Feb.) and a much smaller difference during summer (June to Aug.). In winter, the
468 temperature gradient above the fracture depth was quite low (between 0.5 and 0.9°C m⁻¹
469 between 0.3 and 2.5 m, depending on the year), but much higher at greater depth (between 5.1
470 and 6°C m⁻¹ between 2.5 and 3 m, 6.3°C m⁻¹ between 3 and 4 m, and >4°C.m⁻¹ down to 7 m).
471 In summer the difference in temperature gradients was much less marked, although there was
472 still a substantial change in temperature gradient at the fracture depth. The mean gradient
473 stepped up from between -1.4°C and -2°C m⁻¹ between 0.3 to 2-m-depth, to between -2.3 to -
474 5.1°C m⁻¹ between 2 and 2.5-m-depth. The temperature gradient remained relatively high (>
475 2.4°C.m⁻¹ except in 2010) up to 4-m-depth, and then progressively decreased. These
476 observations suggest that the fracture provokes a heat sink, with greater downward
477 propagation in winter, and a more localized effect in summer. This cooling effect may be due
478 to air ventilating through the open fracture, a process that has been shown to have an
479 important cooling effect on steep rock wall permafrost (Hasler et al. 2011a). In our study this
480 cooling effect was greater when the air temperature was low. Nevertheless, despite this this
481 cooling effect, water percolation can occur along the fracture and heat advection could locally
482 warm the rock (Hasler et al. 2011b). However, the temperature data for BH_N do not provide
483 any evidence for this. The temperature profile for BH_E is generally linear indicating that
484 conduction is the dominant heat transfer process (Williams and Smith, 1989). Thus, active
485 layer thickness and timing and permafrost temperatures at the AdM are controlled by a
486 number of factors that interact with each other, including snow cover, latent heat consumption
487 (which delays and dampens short-term responses to climate signals), and cooling effect due to
488 air ventilation within open fractures.

489

490 **7 Conclusion**

491 The high altitude, morphology, and accessibility of AdM make it an exceptional site for
492 investigating permafrost in steep rock walls. A monitoring network installed on the AdM to
493 investigate the thermal effects of topography, snow cover and fractures on permafrost
494 provided eight years of rock surface temperature and four years of borehole temperature data.
495 The results of our analyses of this new dataset supported the findings of previous field studies
496 and a number of numerical experiments:

- 497 - The thermal characteristics of the AdM's rock walls are typical of steep bedrock
498 permafrost. The spatial variability of surface temperature, active layer thickness
499 and timing, and the permafrost thermal regime are mainly controlled by
500 topography.
- 501 - Borehole temperature data confirm the characteristics of the sub-surface thermal
502 regime predicted by numerical experiments, in particular the coexistence within a
503 single rock peak of warm and cold permafrost, which generates lateral heat fluxes
504 from warm to cold faces.
- 505 - MAGST around a single rock peak is controlled by micro-meteorological
506 parameters (variable cloud formation from year-to-year) when the rock face is
507 snow free, and by local accumulations where there is snow on the face. Snow-free
508 areas and snow-covered areas can show opposite trends.
- 509 - Surface temperature data confirm that thin (not-insulating) snow cover can lower
510 the surface temperature due to the low snow surface albedo.

511 Our results also extended the results of previous studies:

- 512 - Sensors with thick snow cover showed evidence of a similar thermo-insulation
513 effect to that found on gentle mountain slopes, with smoothing of daily
514 temperatures in winter, a melting period marked by constant surface temperature
515 of around 0°C, reduced freezing of the active layer in winter, and delayed thawing
516 of the active layer in summer.
- 517 - Thick snow accumulations warm MAGST of shady areas and increases
518 interannual differences compared with sunny areas which are cooled by snow
519 blocking solar radiation, and where interannual differences are reduced by the
520 balance between the opposite effects of thermo-insulation and strong albedo.
- 521 - Open fractures have a strong, localized cooling effect, possibly due to air
522 ventilation within the fracture. This cooling effect is greater in winter and the heat
523 sink mainly affects the 3-4 m below the fracture.

524

525 **8. Further developments**

526 The thermal characteristics of the AdM illustrate the complexity of the processes controlling
527 the thermal regime of shallow layers in rock wall permafrost. Modelling these processes
528 represents a major challenge but the data presented here provide a step towards achieving this
529 goal. Studies into the controlling effect of snow cover are needed in order to determine the
530 impact of thick accumulations and summer snow fall on ALT and permafrost changes. The
531 current research project has already collected a large amount of data, including picture
532 showing the evolution of the south and northeast-facing slopes of the AdM, snow-stake

533 measurements, and borehole records. Further analyses of these data would help improve
534 understanding of rock fall activity. Research into latent heat consumption in compact bedrock
535 may also provide insight into ALT thickness and timing on some snow-covered rock walls,
536 and into permafrost evolution over short-time scales. The BH_N fracture could be used to
537 investigate non-conductive heat transfers, for example by developing a heat conduction
538 scheme. Ground-penetrating radar measurements of the northwest-facing slope, including
539 BH_N, offer a detailed picture of the bedrock discontinuities and provide useful additional
540 data for developing a heat flow model integrating bedrock structure. The combined use of
541 crack-meters, air temperature measurements, and borehole data provides a promising avenue
542 for developing understanding of the thermal and mechanical factors affecting rock wall
543 instabilities.

544 The dataset presented here was used for evaluation of statistical and numerical models
545 designed to map the distribution of permafrost in the Mont Blanc Massif (Magnin et al., 2014)
546 and to predict the distribution and evolution of the temperature field at the AdM over the next
547 century (Noetzli et al., 2014b). The statistical model will be used to determine bedrock
548 temperatures and the related permafrost thermal regime at rock fall locations in order to
549 analyze the relationship between bedrock temperature and rock failures.

550

551 *Acknowledgements:* We would like to thank S. Gruber, U. Morra di Cella, E. Cremonese, and
552 E. Malet, for their help with equipment installation and data acquisition at the Aiguille du
553 Midi. The Chamonix *Compagnie des Guides* provided invaluable assistance with the drilling
554 operations. We would also like to thank the *Compagnie du Mont Blanc* (especially E.
555 Desvaux) for allowing access to the site, and Météo France for providing air temperature data.
556 Thank you to A. Hasler and anonymous reviewer for their useful comments and
557 recommendations. The english text was corrected by P. Henderson. This work was supported
558 by the Region Rhône-Alpes (*CIBLE* program).

559 **References**

560

561 Allen, S. K., Gruber, S., and Owens, I. F.: Exploring steep bedrock permafrost and its
562 relationship with recent slope failures in the Southern Alps of New Zealand, *Permafrost*
563 *Periglac.*, 20, 345–356, doi:10.1002/ppp.658, 2009.

564

565 Boeckli, L., Brenning, A., Gruber, S., and Noetzli, J. Permafrost distribution in the European
566 Alps: calculation and evaluation of an index map and summary statistics. *The Cryosphere*
567 *Discuss.*, 6, 849–891, doi:10.5194/tcd-6-849-2012, 2012.

568

569 Deline, P.: Recent Brenva rock avalanches (Valley of Aosta): new chapter in an old story?
570 *Supplementi di Geografia Fisica e Dinamica Quaternaria*, 5, 55–63, 2001.

571

572 Deline, P., Alberto, W., Broccolato, M., Hungr, O., Noetzli, J., Ravanel, L., and Tamburini,
573 A.: The December 2008 Crammont rock avalanche, Mont Blanc massif area, Italy, *Nat.*
574 *Hazard Earth Sys.*, 11, 3307–3318, 2011.

575

576 Deline, P., Gardent, M., Magnin F., and Ravanel, L.: The morphodynamics of the Mont Blanc
577 massif in a changing cryosphere: a comprehensive review, *Geogr. Ann. A*, 94(2), 265–283,
578 2012.

579

580 Fischer, L., Käab, A., Huggel, C., and Noetzli, J.: Geology, glacier changes, permafrost and
581 related slope instabilities in a high-mountain rock wall: Monte Rosa east face, Italian Alps,
582 *Nat. Hazard Earth Sys.*, 6, 761–772, 2006.

583

584 Gruber, S. and Haeberli, W.: Permafrost in steep bedrock slopes and its temperature related
585 destabilization following climate change, *J. Geophys. Res-Earth.*, 112, F02S13,
586 doi:10.1029/2006JF000547, 2007.

587

588 Gruber S. and Haeberli W.: Mountain permafrost, in: *Permafrost soils, Margesin R*, Springer,
589 16, 33-44, 2009.

590

591 Gruber, S., Peter, M., Hoelzle, M., Woodhatch, I., and Haeberli, W.: Surface temperatures in
592 steep alpine rock faces: a strategy for regional-scale measurement and modelling, in:
593 *Proceedings of the 8th International Conference on Permafrost*, L. Arenson, Zürich, 325-330,
594 2003.

595

596 Gruber, S., Hoelzle, M., and Haeberli, W.: Permafrost thaw and destabilization of Alpine rock
597 walls in the hot summer of 2003, *Geophys. Res. Lett.*, 31, L13504,
598 doi:10.1029/2004GL0250051, 2004a.

599

600 Gruber, S., Hoelzle, M., and Haeberli, W.: Rock-wall temperatures in the Alps: modelling
601 their topographic distribution and regional differences, *Permafrost Periglac.*, 15, 299–307,
602 doi: 10.1002/ppp.501, 2004b.

603

604 Gubler, S., Fiddes, J., Keller, M., and Gruber, S.: Scale-dependent measurement and analysis
605 of ground surface temperature variability in alpine terrain, *The Cryosphere*, 5, 431–443, 2011.

606

607 Hanson, S. and Hoelzle, M.: The thermal regime of the active layer at the Murtèl rock glacier
608 based on data from 2002. *Permafrost Periglac.*, 15, 273–282, doi: 10.1002/ppp.499, 2004.

609

610 Harris, S. and Corte, A.: Interactions and relations between mountain permafrost,
611 glaciers, snow and water, *Permafrost Periglac.*, 3, 103–110, 1992.

612

613 Hasler, A., Gruber, S., and Haeberli, W.: Temperature variability and offset in steep alpine
614 rock and ice faces, *The Cryosphere*, 5, 977–988, doi:10.5194/tc-5-977-2011, 2011a.

615

616 Hasler, A., Gruber, S., Font, M., and Dubois, A.: Advective heat transport in frozen rock
617 clefts - conceptual model, laboratory experiments and numerical simulation. *Permafrost*
618 *Periglac.*, 22, 378–349, doi: 10.1002/ppp.737, 2011b.

619

620 Hipp, T., Etzelmüller, B. and Westermann, S.: Permafrost in Alpine Rock Faces from
621 Jotunheimen and Hurrungane, Southern Norway. *Permafrost Periglac.*, 25: 1–13.
622 doi: 10.1002/ppp.1799, 2014.

623

624 Hoelzle, M., Wegmann, M., and Krummenacher, B.: Miniature temperature dataloggers for
625 mapping and monitoring of permafrost in high mountain areas: first experience from the
626 Swiss Alps. *Permafrost Periglac.*, 10: 113–124. doi: 10.1002/(SICI)1099-
627 1530(199904/06)10:2<113::AID-PPP317>3.0.CO;2-A, 1999.

628

629 Huggel, C., Caplan-Auerbach, J., and Wessels, R.: Recent extreme avalanches triggered by
630 climate change, *EOS, Transactions American Geophysical Union*, 89, 469–470, 2008.

631

632 Huggel, C., Zraggen-Oswald, S., Haeberli, W., Kääh, A., Polkvoj, A., Galushkin, I., and
633 Evans, S.G.: The 2002 rock/ice avalanche at Kolka/Karmadon, Russian Caucasus: assessment
634 of extraordinary avalanche formation and mobility, and application of Quick- Bird satellite
635 imagery, *Nat. Hazard Earth Sys.*, 5, 173–187, doi:10.5194/nhess-5-173-2005, 2005.

636

637 Krautblatter, M., Huggel, C., Deline, P., and Hasler, A.: Research Perspectives on Unstable
638 High-alpine Bedrock Permafrost: Measurement, Modelling and Process Understanding.
639 *Permafrost Periglac.*, 23, 80–88, DOI: 10.1002/ppp.740 2011.

640

641 Juliussen, H. and Humlum, O.: Towards a TTOP ground temperature model for mountainous
642 terrain in central-eastern Norway. *Permafrost Periglac.*, 18, 161–184, doi: 10.1002/ppp.586,
643 2007.

644

645 Kukkonen, I. T. and J. Safanda.: Numerical modelling of permafrost in bedrock in northern
646 Fennoscandia during the Holocene, *Global Planet. Change*, 29, 259– 273, 2001.

647

648 Leloup, P. H., Arnaud, N., Sobel, E. R., and Lacassin, R.: Alpine thermal and structural
649 evolution of the highest external crystalline massif: The Mont Blanc. *Tectonics*, 24, TC4002,
650 doi: 10.1029/2004TC001676, 2005.

651

652 Le Roy, M.: Reconstitution des fluctuations glaciaires holocènes dans les Alpes occidentales,
653 Thèse de Doctorat de Géographie, Université de Savoie, Le Bourget du Lac, 344 pp, 2012.

654

655 Luetschg, M., Lehning, M., and Haeberli, W.: A sensitivity study of factors influencing
656 warm/thin permafrost in the Swiss Alps, *J. Glaciol.*, 54, 696–704, 2008.

657

658 Magnin, F., Brenning, A., Bodin, X., Deline, P., Ravanel, L.: Statistical modelling of rock
659 wall permafrost distribution: application to the Mont Blanc massif, *Géomorphologie*,
660 Manuscript submitted.

661

662 Noetzli, J., Gruber, S., Kohl, T., Salzmann, N., and Haeberli, W.: Three-dimensional
663 distribution and evolution of permafrost temperatures in idealized high-mountain topography,
664 *J. Geophys. Res-Earth*, 112, F02S13, doi:10.1029/2006JF000545, 2007.

665

666 Noetzli, J., Christiansen, H. H., Guglielmin, M., Romanovsky, V. E., Shiklomanov, N. I.,
667 Smith, A.L., and Zhao, L.: Permafrost thermal state, in: *State of the Climate in 2013*, *Bull.*
668 *Amer. Meteor. Soc.*, 95, 2014a.

669

670 Noetzli, J., Ravanel L., and Deline P.: Combining measurements and modelling to describe
671 the permafrost conditions at the Aiguille du Midi (3842 m asl, Mont Blanc Massif). *The*
672 *Cryosphere*, in preparation.

673

674 PERMOS: Permafrost in Switzerland 2002/2003 and 2003/2004, in: Vonder Mühl, D. (eds.),
675 *Glaciological Report (Permafrost) No. 4/5 of the Cryospheric Commission of the Swiss*
676 *Academy of Sciences, Zürich*, 121 pp, 2007.

677

678 PERMOS: Permafrost in Switzerland 2008/2009 and 2009/2010, in: Noetzli, J. (eds.),
679 *Glaciological Report (Permafrost) No. 10/11 of the Cryospheric Commission of the Swiss*
680 *Academy of Sciences, Zürich*, 95 pp, 2013.

681

682 Pogliotti, P.: Influence of Snow Cover on MAGST over Complex Morphologies in Mountain
683 Permafrost Regions. PhD thesis, Turin, Italy, Università degli Studi di Torino, 79 pp, 2011.

684

685 Ravanel, L. and Deline P.: Climate influence on rockfalls in high-Alpine steep rock walls: the
686 north side of the Aiguilles de Chamonix (Mont Blanc massif) since the end of the ‘Little Ice
687 Age’, *The Holocene*, 21, 357–365, doi: 10.1177/0959683610374887, 2010.

688

689 Ravanel, L., Allignol, F., Deline, P., Gruber, S., and Ravello, M.: Rock falls in the Mont
690 Blanc Massif in 2007 and 2008, *Landslides*, 7, 493–501, 2010.

691

- 692 Ravanel, L., Deline, P., Lambiel, C., and Vincent C.: Intability of a high Alpine rock ridge:
693 the lower Arête des Cosmiques, Mont Blanc massif, France, *Geogr. Ann. A*, 95, 51–66, doi:
694 10.1111/geoa.12000, 2012.
- 695
- 696 Romanovsky, V. E., Smith, S. L., Christiansen, H. H., Shiklomanov, N. I., Streletskiy, G. A.,
697 Drozdov, D. S., Malkova, G. V., Oberman, N. G., Kholodov, A. L., and Marchenko, S. S.:
698 [Terrestrial permafrost, in: *State of the Climate in 2013*, *Bull. Amer. Meteor. Soc.*, 95, S139–
699 S141, 2014.
- 700
- 701 Smith, M. W. and Riseborough, D. W.: Permafrost monitoring and detection of climate
702 change. *Permafrost Periglac.*, 7, 301–309, doi: 10.1002/(SICI)1099-
703 1530(199610)7:4<301::AID-PPP231>3.0.CO;2-R, 1996.
- 704
- 705 Smith, M. W. and Riseborough, D. W.: Climate and the limits of permafrost: a zonal analysis.
706 *Permafrost Periglac.*, 13, 1–15, doi: 10.1002/ppp.410, 2002.
- 707
- 708 Williams, P. J. and Smith, M. W.: *The frozen earth*, *Studies in polar research*, Cambridge
709 University Press, Cambridge, 306 pp., 1989.

710 **Tables**

711

Site Code	Elevation [m a.s.l.]	Aspect [°]	Slope [°]	Sensor depths [m]	Estimated snow accumulation [m]
BH_S	3753	135	55	0.14, 0.34, 0.74, 1.04, 1.34, 1.64, 2.14, 2.64, 3.64, 4.64, 6.64, 8.64, 9.64	> 0.8
BH_N	3738	345	90	0.3, 0.5, 0.7, 0.9, 1.1, 1.4, 1.7, 2, 2.5, 3, 4, 5, 7, 9, 10	> 1.0
BH_E	3745	50	65	0.3, 0.5, 0.7, 0.9, 1.1, 1.4, 1.7, 2, 2.5, 3, 4, 5, 7, 9, 10	< 0.6
W1	3825	270	80	0.1	0
S1	3820	140	74	0.1	0
N1	3820	354	84	0.1	0
E1	3823	124	60	0.1	0
N2	3820	334	80	0.03, 0.1, 0.3, 0.55	0
E2	3820	118	60	0.03, 0.1, 0.3, 0.55	0
S2	3815	160	85	0.03, 0.1, 0.3, 0.55	0
W2	3825	270	85	0.03, 0.1, 0.3, 0.55	0
S3	3820	158	70	0.03, 0.1, 0.3, 0.55	0.5 to 1.0
AT	3845	0	0		0

712 **Table 1.** Instrument positions.

713 BH: borehole thermistor chains, X1 and X2: rock surface temperature loggers, AT: air
714 temperature. Estimated snow accumulation: from automatic cameras and probes for BH_S
715 and BH_E (winter 2012 and 2013), from field observation for S3 and BH_N.

Year	2006				2007				2008				2009				2010				2011				2012				2013			
Season	Wi	Sp	Su	Fa	Wi	Sp	Su	Fa	Wi	Sp	Su	Fa	Wi	Sp	Su	Fa	Wi	Sp	Su	Fa	Wi	Sp	Su	Fa	Wi	Sp	Su	Fa	Wi	Sp	Su	Fa
N1	[Dark Blue]																[Light Blue]															
E1	[Dark Blue]																[Light Blue]															
S1	[Dark Blue]																[Light Blue]															
W1	[Dark Blue]																[Light Blue]															
N2	[Dark Blue]				[Dark Blue]				[Dark Blue]				[Dark Blue]				[Dark Blue]				[Dark Blue]											
E2	[Dark Blue]				[Dark Blue]				[Dark Blue]				[Dark Blue]				[Dark Blue]				[Dark Blue]											
S2	[Dark Blue]				[Dark Blue]				[Dark Blue]				[Dark Blue]				[Dark Blue]				[Dark Blue]											
W2	[Dark Blue]				[Dark Blue]				[Dark Blue]				[Dark Blue]				[Dark Blue]				[Dark Blue]											
S3	[Dark Blue]				[Dark Blue]				[Dark Blue]				[Dark Blue]				[Dark Blue]				[Dark Blue]											
BH_S	[Dark Blue]								[Dark Blue]								[Dark Blue]															
BH_E	[Dark Blue]								[Dark Blue]								[Dark Blue]															
BH_N	[Dark Blue]								[Dark Blue]								[Dark Blue]															
AT	[Dark Blue]																[Dark Blue]															

717 **Table 2.** Data availability after gap filling.

718 **Wi:** December, January, February; **Sp:** March, April, May; **Su:** June, July, August; **Fa:**
 719 September, October, November.

720 Red sections indicate where gaps <1.5 month per year have been filled in order to calculate
 721 annual means but seasonal means were not calculated for the seasons in question. The time
 722 series interrupted with white gap areas indicate that annual mean is not computed for the
 723 concerned year.

Year	BH_E			BH_S			BH_N			MAAT
	ALT [m]	Max. ALT [dd.mm]	MART _{10m} [°C]	ALT [m]	Max. ALT [dd.mm]	MART _{10m} [°C]	ALT [m]	Max. ALT [dd.mm]	MART _{10m} [°C]	
2010	3.1	27.07	-	5.2	23.10	-1.4	1.8	28.08	-4.7	-9
2011	2.7	30.08	-3.8	5.9	22.10	-1.5	2.3	18.09	-4.6	-6.7
2012	3.3	26.08	-3.6	-	-	-	2.5	26.08	-4.3	-7.7
2013	3.4	08.09	-3.6	5.8	30.09	-	2.2	25.08	-4.5	-

724 **Table 3.** Borehole and air temperature records.

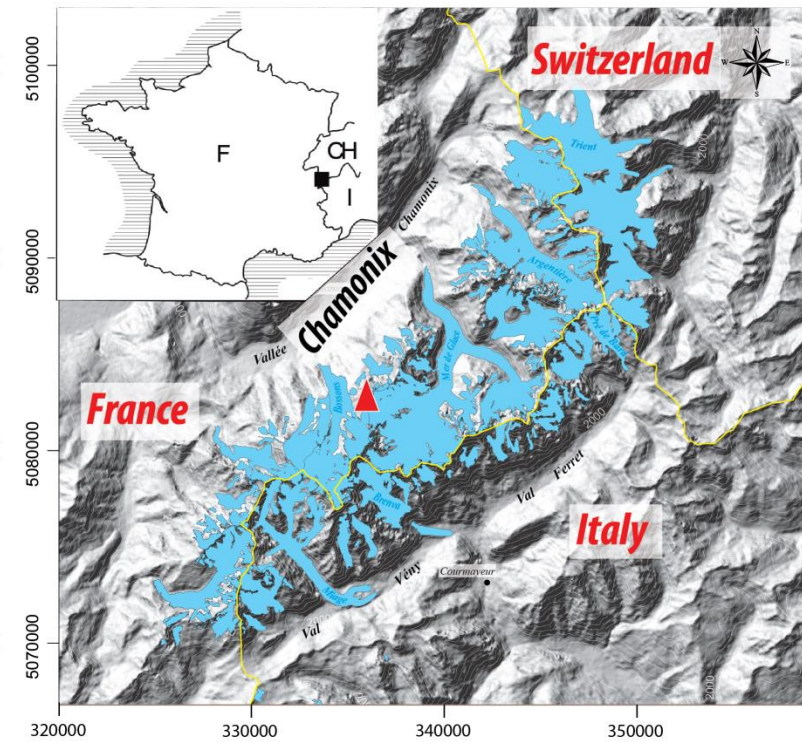
725 ALT: Active Layer Thickness

726 MART_{10m}: Mean Annual Rock Temperature at 10-m depth

727 MAAT: Mean Annual Air Temperature

728

729 **Figures**



730

731

732 **Figure 1.** Location of the Mont Blanc Massif and the Aiguille du Midi (red triangle)
733 (modified from Le Roy, 2012).

734

735

736

737

738

739

740

741

742

743

744

745



746

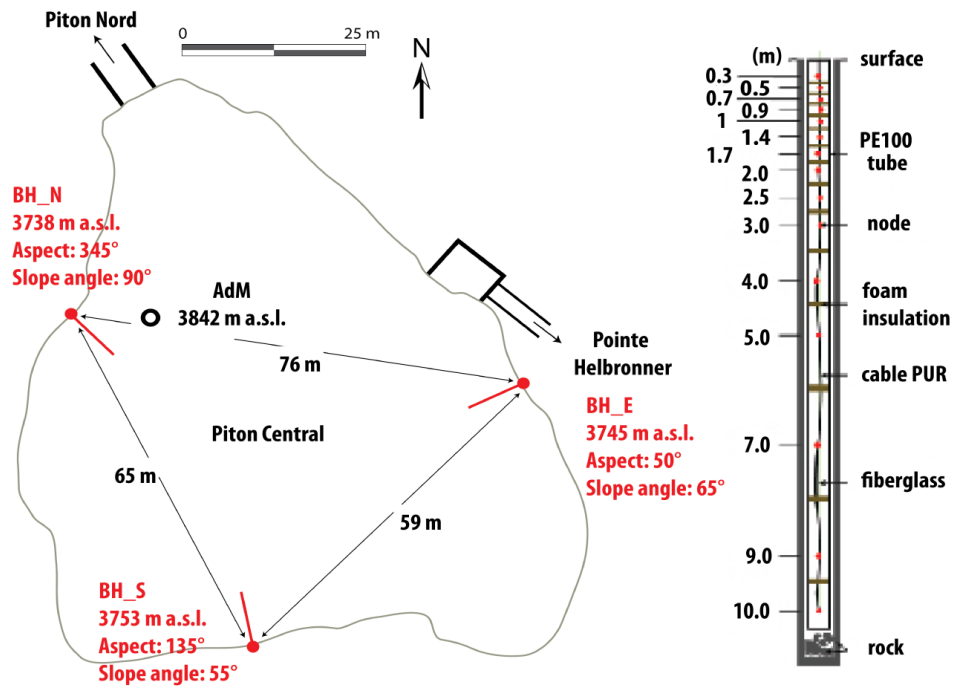
747

748 **Figure 2.** The Aiguille du Midi with snow camera, air temperature, rock surface temperature,
 749 and borehole logger locations.

750 *Pictures: S. Gruber (top left and right, bottom left); P. Deline (bottom right).*

751

752

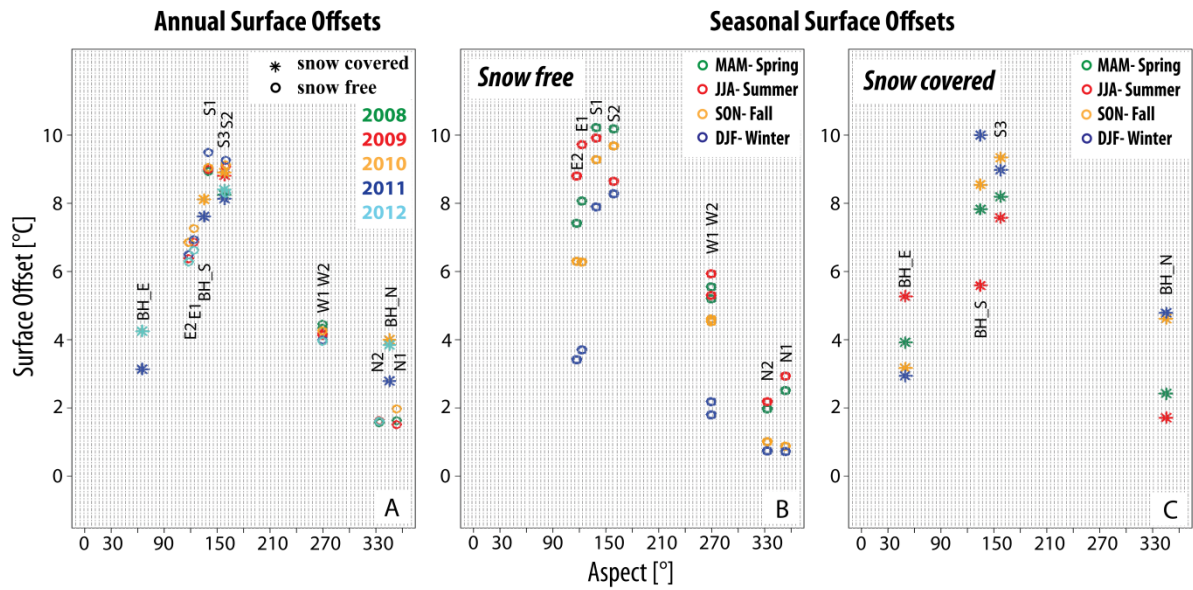


753
 754
 755
 756
 757
 758
 759
 760
 761
 762
 763
 764
 765
 766
 767
 768

Figure 3. Borehole positions and components.

Left: Horizontal cross-section through the AdM's Piton Central. Borehole positions are marked in red.

Right: 10-m-long, 15-node thermistor chain installed in the boreholes.

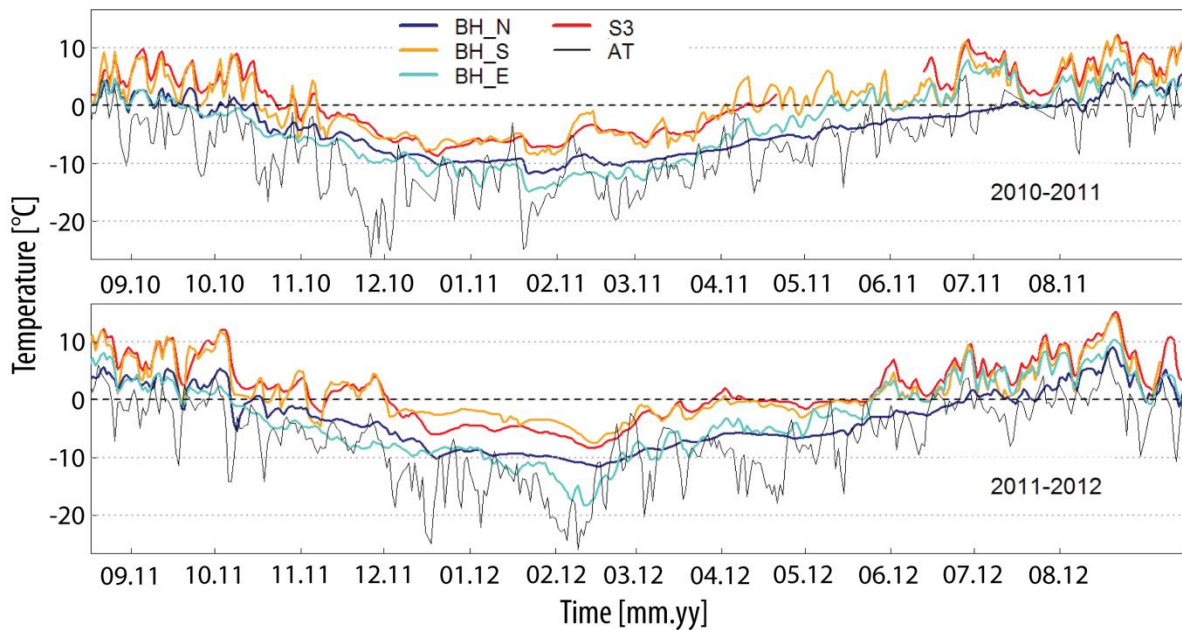


769

770 **Figure 4.** Annual and Seasonal Surface Offsets calculated from sensors at 0.3-m depth.

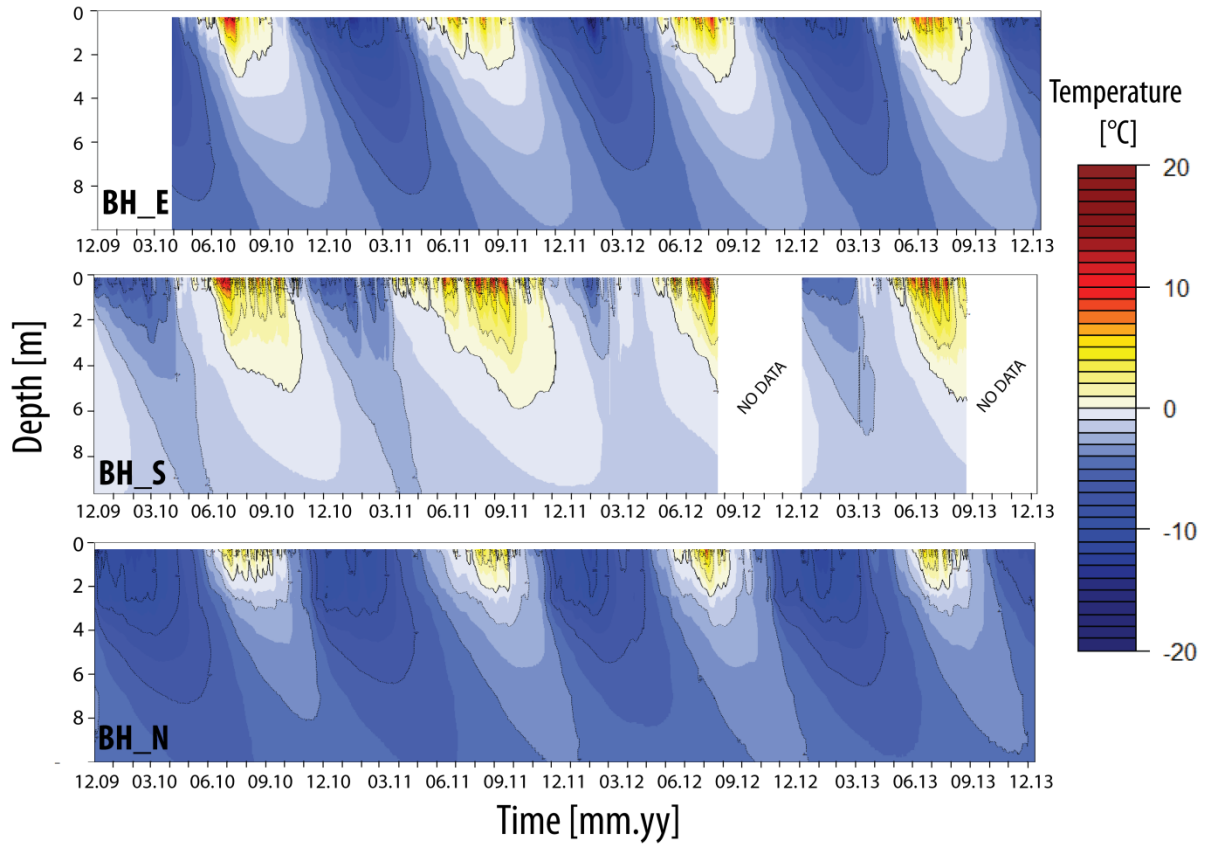
771 ASOs are shown for all the available years. SSOs are the mean values for the available
 772 seasons for each logger listed in Table 2.

773



774

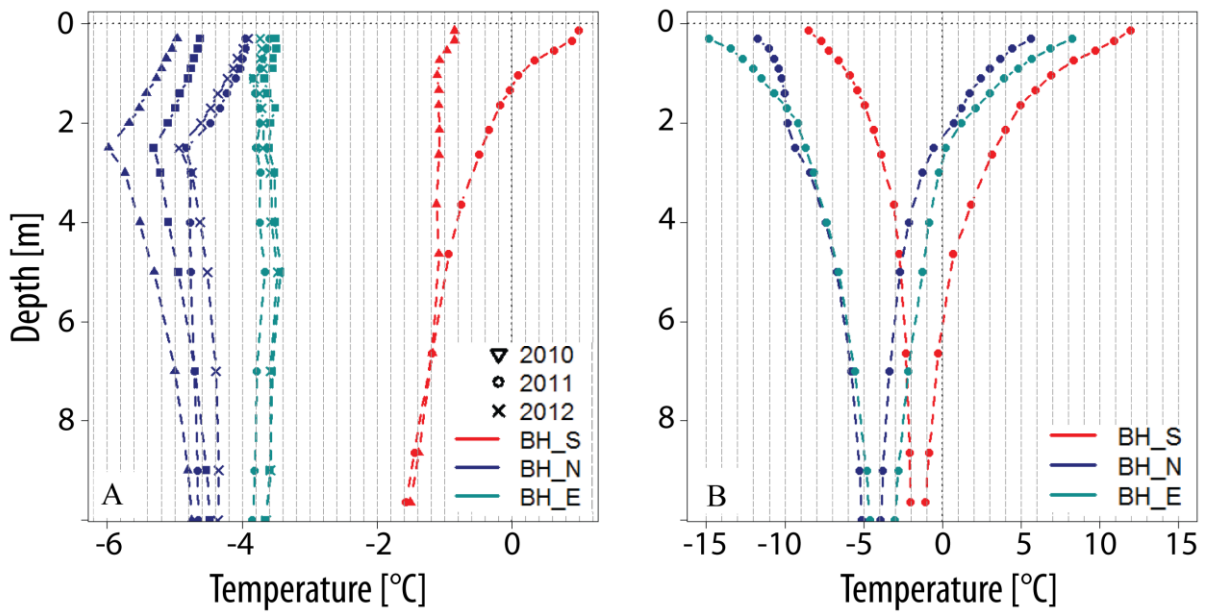
775 **Figure 5.** Daily temperature records at 0.3-m depth for snow-covered sensors for the 2010-
 776 2011 and 2011-2012 hydrological years.



777

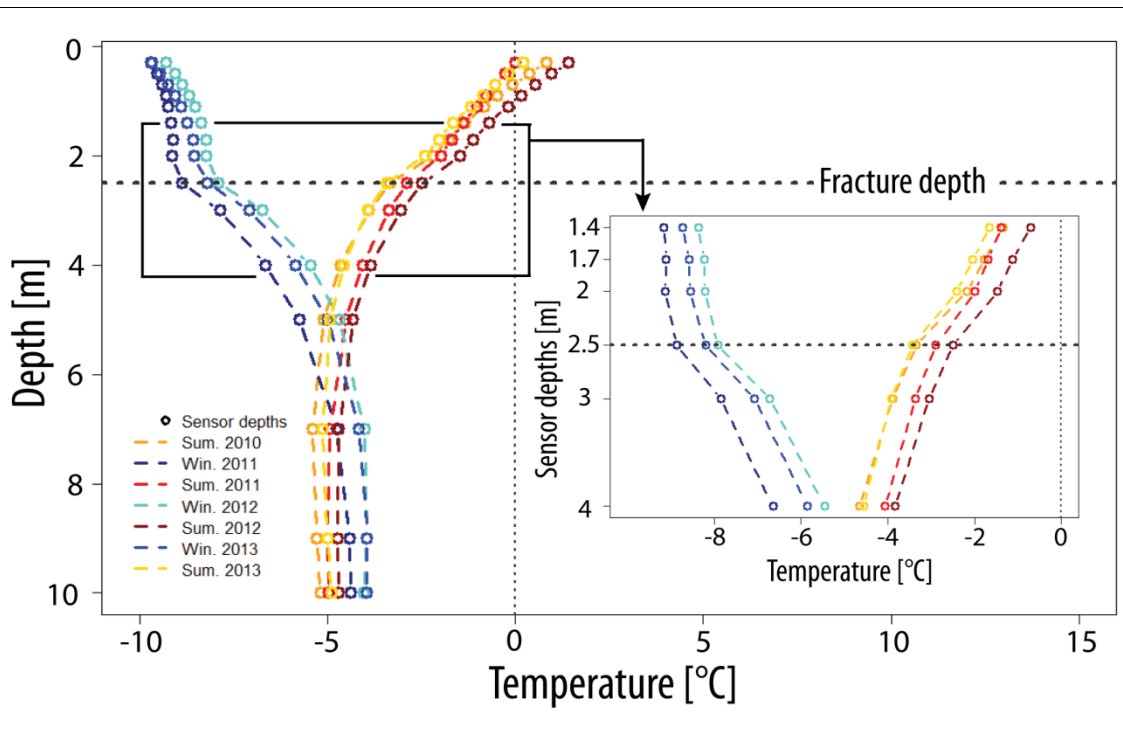
778 **Figure 6.** Daily temperature records in the AdM boreholes from December 2009 to December
 779 2013.

780



781

782 **Figure 7.** Mean $T(z)$ profiles (A) and 2011 temperature envelopes (B) of the AdM boreholes.



783

784 **Figure 8.** Seasonal $T(z)$ profiles for winters (December to February) and summers (June to
 785 August) recorded in BH_N.